Reactive and Functional Polymers 218 (2026) 106526

Contents lists available at ScienceDirect

Reactive and Functional Polymers

journal homepage: www.elsevier.com/locate/react

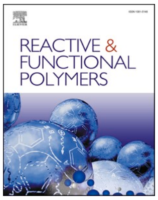

The influence of RAFT agent on the properties of anion exchange membrane with well-controlled graft structure for fuel cell applications

Yasko Kodama [*,1], Andrey S. Barbosa [1], Bianca P.S. Santos, Marcelo Linardi, Elisabete I. Santiago [*]

Nuclear and Energy Research Institute, IPEN/CNEN, 05508-000 São Paulo, Brazil

ARTICLE INFO

Keywords:
Anion-exchange membrane
RAFT
radiation-induced grafting
AEMFC

ABSTRACT

Reversible addition–fragmentation chain transfer (RAFT) agents can be employed to control radical polymerization processes in the synthesis of anion-exchange membranes (AEMs) via radiation-induced grafting (RIG). However, the influence of the RAFT agent content on the performance of anion-exchange membrane fuel cells (AEMFCs) remains largely unexplored. Herein, we present a flexible method for AEM preparation that combines the radiation chemistry of polymers with RAFT polymerization. Low-density polyethylene (LDPE) films were simultaneously irradiated with vinylbenzyl chloride (VBC) monomer and RAFT agent to achieve rigorous control over the molecular weight of the grafted side chains. The incorporation of RAFT agent into the LDPE-grafted polymer chains significantly reduced the degree of grafting, and gel permeation chromatography (GPC) measurements confirmed the reduction in molecular weight. Cross-sectional Raman microscopy revealed that the RAFT protocol also improved graft homogeneity across the polymer matrix. Furthermore, the mechanical properties and surface morphology of the resulting AEMs were enhanced by the use of the RAFT method. The membranes were subsequently characterized in terms of ion-exchange capacity, water uptake, in-plane and through-plane swelling, thermal stability, and hydroxide conductivity. Single-AEMFC tests, as well as chemical stability measurements, demonstrated that RAFT-based AEMs maintained high performance (~1.3 W·cm^{-2}), while exhibiting a markedly lower IEC loss (~30 %) compared to non-RAFT AEMs, thus contributing significantly to AEMFC stability.

1. Introduction

Anion exchange membrane fuel cells (AEMFCs) have recently attracted considerable interest as a viable alternative to conventional proton exchange membrane fuel cells (PEMFCs). By enabling the use of non-precious metal catalysts, AEMFCs have been considered a substitute to conventional alkaline fuel cells with a competitive cost-effectiveness. In AEMFCs, a polymer electrolyte (anion exchange membrane, AEM) conducts hydroxide ions (OH^-) instead of protons (H^+), favoring the kinetic of electrode reactions, such as oxygen reduction reaction (ORR) [1–6]. Moreover, operation in alkaline medium mitigates corrosion issues associated with acidic environments, enhancing the durability and stability of the cell components. Despite these advantages, challenges, such as improving the performance and stability of the anion exchange membranes (AEM), optimizing water management, and enhancing catalyst activity remain critical research areas [7–10].

Anion-exchange membranes (AEM) represent an important class of ionomeric materials composed of non-ionic and ionic phases that conduct anions, such as OH^-, CO_3^{2-}, HCO_3^-, Cl^-. Typically, AEMs are copolymers composed of a polymer backbone, which provides the physical and mechanical properties of the membrane, side chains that support the functional groups, and the functional groups themselves (quaternary ammonium, QA), which act as the ion-conducting sites responsible for anion transport [11–13].

Among the various methods available for producing AEMs, the copolymerization of monomers onto engineering polymers by radiation-induced grafting (RIG) has proven to be particularly effective [14–19]. RIG represents a versatile strategy, wherein radicals are generated within a prefabricated polymer matrix and subsequently exploited to anchor monomers through irradiation, enabling precise tailoring of membrane functionality. Several polymer types have been used to synthesize AEMs, such as fluorinated (Polytetrafluoroethylene (PTFE), Poly

---

* Corresponding authors.
E-mail addresses: yasko.kodama@gmail.com (Y. Kodama), elisabete.santiago@usp.br (E.I. Santiago).

[1] Both authors contributed equally to this work.

https://doi.org/10.1016/j.reactfunctpolym.2025.106526
Received 11 June 2025; Received in revised form 9 October 2025; Accepted 20 October 2025

(tetrafluoroethylene-*co*-hexafluoropropylene) (FEP), partially fluorinated (Poly(ethylene-*co*-tetrafluoroethylene) (ETFE) and non-fluorinated polymers as polyethylene [14,17,19]. Low-density polyethylene (LDPE) is particularly interesting due to its thermoplastic characteristic combined with low cost, good physicochemical properties, such as thermal stability, and recyclability [1].

Despite the recurrent use of LDPE as a polymer matrix in AEMs produced by RIG, some limitations, such as performance and durability, still require improvements in both processing techniques and the development of novel structural and morphological configurations. A key limitation of RIG, which employs conventional radical polymerization (FRP), is the lack of precise control over the ratio of functional groups grafted onto the polymer backbone. Therefore, the development of AEMs with properties specifically designed for electrochemical device applications is highly desirable [18]. For this reason, surface modification by RIG through controlled radical polymerization (CRP) is one technique to be exploited for the synthesis of graft copolymers.

In this context, the reversible addition–fragmentation chain-transfer (RAFT) method (recently labeled as reversible deactivation radical polymerization (RDRP) by IUPAC, 2025) emerges as an alternative technique, able to tailoring chemical and physical properties of interfaces and surfaces of a polymer and represents a good choice for CRP [3,20–22]. In addition, a careful selection of RAFT agents enables the polymerization of a wide range of vinyl monomers under optimal reaction conditions. Furthermore, the combination of RIG and the RAFT method can result in AEMs with well-controlled structures, contributing to achieving suitable properties for AEMFC application.

This work focuses on the preparation of AEMs based on LDPE with controlled side-chain molecular weight via RAFT agent incorporated in the RIG approach. The resulting membranes were characterized in terms of molecular structure, physicochemical, thermal and mechanical properties, surface morphologie, hydroxide conductivity and subsequently assessed as polymeric electrolyte in H_2/O_2 AEMFCs.

2. Experimental

2.1. Materials

Commercial low-density polyethylene films (LDPE, 25 μm, Goodfellow) were used as the polymeric matrix. Vinylbenzyl chloride monomer (VBC, a mixture of 2-, 3-, and 4-isomers, 97 %), RAFT agent cyanomethyl dodecyl trithiocarbonate (CMDTC), and trimethylamine (TMA, 25 % *v*/v) were purchased from Sigma-Aldrich. Toluene, potassium hydroxide, acetone, ethanol, and sodium chloride were of analytical reagent grade and used as received.

2.2. Membranes preparation

AEMs were prepared following the procedure shown in the scheme illustrated in Fig. 1. For the grafting step, LDPE films and different amounts of RAFT agent (0, 56 and 112 mg) were placed in a screw-cap vial containing a mixture of VBC/toluene/ethanol (27/28/45 vol%). The vial set was purged with pure nitrogen (99.995 %) for 5 min to remove air. A Gammacell 220 ^{60}Co source was used to irradiate the samples with a total absorbed dose of 25 kGy at a dose rate of 0.4 kGy h^{-1}. Immediately after irradiation, the LDPE-grafted films were washed several times with toluene and acetone to ensure removal of homopolymers and RAFT agent residues. As a sequence, LDPE-grafted films were dried at room temperature (RT) overnight. The degree of grafting (DoG) was estimated using Eq. 1.

$$\mathrm{DoG} = \frac{Wf - W_i}{W_i} x100\% \tag{1}$$

where W_f is the LDPE-grafted film weight, and W_i (g) is the weight of pristine LDPE.

After grafting process, the LDPE-grafted films were aminated with aqueous TMA solution (25 % vol.) for 24 h at RT [23]. The resulting

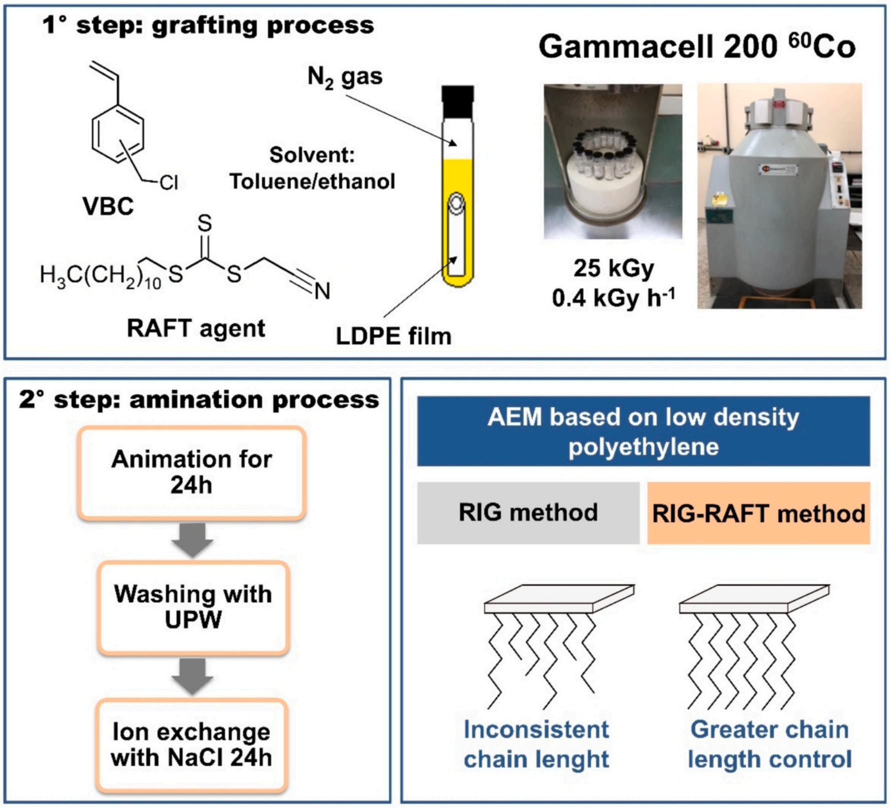

Fig. 1. The schematic processes used for the preparation of AEMs by RIG-RAFT method.

AEMs were exhaustively washed with ultrapure water (UPW) and stored in chloride form (LDPE-AEM Cl^-) in ultrapure water (UPW).

Non-RAFT and RAFT AEMs were labeled as follows: LG-0 (L = LDPE, G = grafting, 0 = without RAFT agent), LG-56 (L = LDPE, G = grafting, RAFT agent = 56 mg), and LG-112 (L = LDPE, G = grafting, RAFT agent = 112 mg).

Water uptake (WU), in-plane swelling (IPS), and through-plane swelling (TPS) of the AEMs in chloride (Cl^-) and hydroxide (OH^-) forms were determined. It is important mentioning that measurements conducted in OH^- form are more susceptible to carbonation during handling due to reaction of OH^- and atmospheric CO_2, which can lead to inaccurate results. Therefore, some experiments were carried out using AEMs in the Cl^- form.

For measurements in the wet state, AEMs in the Cl^- form (3×3 cm^2) were fully hydrated and equilibrated in UPW for 24 h at room temperature (25 °C). Excess surface water was gently removed with filter paper, and the wet mass, thickness, and area were measured using an analytical balance, micrometer, and digital caliper, respectively. For dry-state measurements, the samples were subsequently dried in a vacuum oven at 50 °C for 16 h.

For the AEMs in OH^- form, fresh specimens were converted by ion exchange in 1 M KOH under stirring for 24 h, followed by thorough rinsing with UPW to eliminate residual electrolyte. In this case, WU, IPS, and TPS were evaluated at 25, 50, and 80 °C. At each temperature, the specimens were conditioned in UPW for 1 h, surface water was quickly removed, and the wet mass, thickness, and area were measured. The samples were then dried in a vacuum oven at 50 °C for 16 h to determine dry values. WU, IPS, and TPS were calculated using Eqs. 2, 3, and 4, respectively:

$$WU = \frac{W_{wet} - W_{dry}}{W_{dry}} x\, 100\% \tag{2}$$

$$IPS = \frac{A_{wet} - A_{dry}}{A_{dry}} x\, 100\% \tag{3}$$

$$TPS = \frac{T_{wet} - T_{dry}}{T_{dry}} x\, 100\% \tag{4}$$

where W_{wet} is the wet weight, W_{dry} is the dry weight, A_{wet} is the wet area, A_{dry} is the dried area, T_{wet} is the thickness of hydrated AEM, and T_{dry} is the thickness of dry AEM. All measurements were performed in triplicate.

The ion exchange capacity (IEC) data were obtained for AEMs in Cl^- form using an automatic titrator (Titrino 848 Plus, Metrohm) equipped with a selective Cl^- electrode, as described elsewhere [23]. The measurement was performed in triplicate, and the value was estimated by using Eq. 5:

$$IEC\ (mmol/g) = \frac{Ep^{*}0.0205}{mdry} \tag{5}$$

where Ep is the end point (mL) taken as the maxima in the first differential plot of the Ag Titrode potential vs. volume data, 0.0205 N is the concentration of the $AgNO_3$ aqueous solution, and m_{dry} is the dry mass of AEM-Cl^- samples.

2.3. Characterization

2.3.1. Gel permeation chromatography (GPC)

Gel permeation chromatography (GPC, Prominence UFLC Shimadzu) was employed to determine the weight average molecular weight (M_w) and the dispersity index (Đ) of the byproduct resulting of grafting reaction from AEMs synthesis. M_w corresponds to the weight-average molecular weight of the polymer, which reflects the contribution of chains of different sizes to the overall mass of the sample. The dispersity index (Đ $=M_w/M_n$) indicates the extent of the molecular weight distribution, with values closer to 1 representing narrower (more uniform) distributions [24].

For GPC analysis, chloroform ($CHCl_3$, HPLC grade) was used as the eluent, and narrow-dispersity polystyrene standards were employed for calibration. The analyses were performed using a Waters Styragel precolumn (4.6 × 30 mm, 500 Å) coupled with two Phenogel 5 μm linear columns (7.8 × 300 mm), covering a separation range of $100–1.0 \times 10^7$ Da. The stationary phase consisted of spherical porous particles of styrene–divinylbenzene copolymers.

2.3.2. Raman spectroscopy

Raman spectroscopy was employed for two main purposes: (i) assessing the chemical structure of the resulting AEMs, and (ii) mapping the distribution of grafts across the cross-section of LDPE-grafted samples.

Raman spectra were collected using a Horiba Jobin Yvon XploRA-PLUS spectrometer equipped with a 785 nm laser (85 mW), a 50× objective lens (NA = 0.50), 5 s exposure time, and 32 accumulations. All spectra were normalized to the 1130 cm^{-1} band, which corresponds to the LDPE backbone.

On the other hand, Raman mapping was carried out on cross-sectional samples prior to the amination step to avoid fluorescence from the TMA groups. In this case, a 785 nm laser (21 mW) was used with a 50× objective lens (NA = 0.50), 5 s exposure time, and 2 accumulations. Raman maps were generated from the ratio of the 1610 cm^{-1} band (VBC groups) to the 1130 cm^{-1} band (LDPE) using LabSpec6 software.

2.3.3. Thermal and mechanical properties

The thermal behavior of the resulting AEMs (LG-0, LG-56, and LG-112) was evaluated by thermogravimetric analysis (TGA) and differential scanning calorimetry (DSC). For TGA, samples (~5 mg) were placed in alumina pans and analyzed using a TG/DTA SDT Q600 instrument (TA Instruments) with a heating rate of 10 °C min^{-1} over the temperature range of 30–600 °C under N_2 flow (100 mL min^{-1}). DSC measurements were performed on a PerkinElmer DSC 6000 instrument. The measurements were carried out in a heating–cooling–heating cycle from 30 to 150 °C at a rate of 10 °C min^{-1} under N_2 flow (50 mL min^{-1}). The melting temperature (Tm) and crystallization temperature (Tc) were determined from the second heating and first cooling scans, respectively.

Mechanical properties were evaluated using a universal testing machine (Instron 5567) at room temperature (~25 °C) equipped with a 1 kN load cell. Rectangular specimens (1×4 cm^2) were previously dried in a vacuum oven at 50 °C. The thickness of each sample was measured at three different points with a Mitutoyo micrometer, and the width was measured at three points with a Mitutoyo digital caliper. A minimum of three specimens were tested for each AEM composition.

2.3.4. Atomic force microscopy (AFM) and scanning electronic microscopy (SEM)

Surface topographic images of the AEMs were obtained by atomic force microscopy (AFM) using an Agilent 5500 AFM/SPM system. Each sample was scanned at a rate of 0.3 lines s^{-1} in soft tapping mode with a NanoWorld Pointprobe® NCST AFM probe with a resonance frequency of 160 kHz and a force constant of 7.4 N m^{-1}.

Surface morphology was further analyzed by scanning electron microscopy (SEM) using a JEOL FESEM JSM-6701F microscope operating at an accelerating voltage of 5 kV. Prior to analysis, the samples were dried in a vacuum oven at 50 °C for 24 h and placed on carbon tape to ensure a uniform surface. No conductive coating was applied to the membranes. The elemental composition (C and Cl) of cross-sectional AEMs was analyzed by using energy-dispersive X-ray spectroscopy (EDS). Cross-sectional samples for EDS were prepared by cutting the membranes with a clean razor blade and mounting the fragments onto carbon tape. All AFM, SEM, and EDS measurements were performed on

AEMs in Cl^- form to avoid handling-related interferences.

2.4. Hydroxide conductivity

Hydroxide conductivity of LG-0, LG-56, and LG-112 was measured by impedance spectroscopy following the methodology proposed by Dekel et al. [25,26]. Each membrane sample (1×4 cm^2) was pretreated by soaking in 1 M KOH for 24 h to ensure complete ion exchange. Afterward, the samples were thoroughly rinsed with ultrapure water (UPW) and placed in a four-probe conductivity cell (BT-112, Scribner Associates).

Conductivity measurements were performed at 30–80 °C under 100 % relative humidity with a constant nitrogen flow of 0.5 mL min^{-1}. Prior to measurement, the samples were subjected to decarbonation at 40 °C by applying a fixed voltage of 0.5 V, generating a current of 800–1000 μA, for 3 h. Subsequently, direct current (DC) voltage sweeps from −0.1 V to 0.1 V were carried out using a potentiostat coupled to a Scribner Associates 850e fuel cell test station. Each sweep was repeated every 10 min for a total of four cycles at each temperature.

The resistance (R) was determined by linear fitting of the voltage–current data and the conductivity was calculated using Eq. 6:

$$\sigma = \frac{d}{R\ x\ w\ x\ t} \tag{6}$$

where d = 0.425 cm, and w and t represent the width and thickness of the hydrated AEM samples, respectively. All measurements were performed on three independent samples ($n = 3$).

2.5. Chemical stability test

Alkaline and oxidative degradation tests were conducted to evaluate AEM stability. For alkaline stability, samples (3×3 cm^2) were immersed in 1 M KOH at 80 °C for 720 h, with weekly solution renewal. After treatment, the membranes were rinsed with UPW and conditioned in 1 M NaCl for 3 days at room temperature under stirring. Alkaline stability was expressed in terms of IEC loss, calculated from the difference between IEC values measured before and after degradation, as described in Section 2.2. All tests were performed in triplicate ($n = 3$).

In addition, oxidative stability was assessed using the Fenton reagent. Samples (2×2 cm^2) were immersed in H_2O_2 solution (3 % v/v) containing 4 ppm $FeSO_4$ at 80 °C. Oxidative degradation was estimated in terms of breaking time, which is defined as the elapsed time from the start of exposure to the Fenton reagent until the first visual evidence of membrane's failure [27].

2.6. Single fuel cell test

Beginning-of-life H_2/O_2 fuel cell tests were performed using gas diffusion electrodes (GDEs). Catalyst inks were prepared by dispersing Pt/C (Alfa Aesar, Johnson Matthey HiSPEC 4000, 40 wt% Pt) for the cathode and PtRu/C (Alfa Aesar, Johnson Matthey HiSPEC 12,100, 40 wt% Pt and 20 wt% Ru) for the anode. Homemade ETFE-based powdered ionomer (AEI, IEC = 2.20 ± 0.01 mmol g^{-1}; synthesis described in the SI), UPW, and isopropanol were added to the catalysts. Each ink was homogenized by ultrasonication for 30 min, spray-coated onto Teflonated Toray TGP-H-60 carbon paper, and dried at 60 °C. The geometric electrode area was 5.0 cm^2. The Pt loading for both anode and cathode was 0.50 ± 0.03 mg cm^{-2}, and the AEI loading was 20 wt%, considering the total solid content.

Prior to fuel cell operation, the electrodes and AEM were immersed in 1 M KOH solution for 30 min to convert AEM and AEI from chloride to the hydroxide form, followed by rinsing with UPW to remove residual ions. The MEA (membrane-electrodes assembly) was assembled in a 5 cm^2 single-cell fuel cell hardware (Scribner Associates, USA) and sealed with a torque of 5.5 N m. Fuel cell performance was evaluated using a Scribner 850e test station. The AEMFC was fed with pure hydrogen (99.999 %) and oxygen (99.998 %) in the anode and cathode, respectively, with flow rate of 1 L min^{-1} under optimized dew point humidification.

A AEMFC short-term durability test in single cell was also performed at 80 °C and 100 % relative humidity, with both gases supplied at 0.3 L min^{-1} for 40 h. The voltage decay was monitored as a function of the time at a fixed current density of 150 mA cm^{-2}.

3. Results and discussion

3.1. Synthesis and molecular structure characterizations

AEMs based on LDPE were prepared using a RAFT agent to control the molecular structure of VBCs graft by RIG method. Traditionally, RIG-based AEMs are prepared by two protocols: pre-irradiation protocol (three steps: irradiation, grafting process, and amination) and simultaneous protocol (two steps: irradiation and grafting process together, and amination) [14]. Here, we incorporate the RAFT agent during the simultaneous protocol to synthesize AEMs. In the classic simultaneous RIG method, γ-irradiation generates radicals both on the LDPE film and in the VBC solution. These radicals promote grafting of VBC onto the film while also enabling homopolymerization of VBC in solution. The prevalence of one process over the other depends on the reaction environment as reagent type, concentration, solvent, temperature, and irradiation atmosphere. Homopolymerization is undesirable because it consumes monomers that could otherwise contribute to grafting. On the other hand, the grafting step attaches side chains to the LDPE backbone, but it is well understood that the classic RIG is not able to control the arrangement of the grafts [28]. Subsequently, after the grafting process, the VBC groups carry the ionic headgroups responsible for anion transport after amination of the AEMs.

In our RIG-RAFT approach, a RAFT agent (varying the amount: 0, 56, and 112 mg) is introduced to control the molecular weight (M_w) and dispersity (Đ) of the grafted poly(VBC) side chains under the same irradiation conditions (25 kGy). In this case, the RAFT agent promotes a new mechanistic route in the simultaneous RIG protocol, such that upon initiation of radicals in the polymer matrix by γ-irradiation (Eqs. 7–8). The propagating radical (P_m^*) adds to the RAFT agent and then fragments (initial equilibrium; Eq. 9) to yield a dormant thiocarbonylthio-capped chain ($P_mS(C{=}S)Z$) and a new radical (R^*). The latter reinitiates polymerization on monomer to form P_n^* (Eq. 10) [29]. A rapid addition–-fragmentation exchange is then established between active radicals and dormant RAFT-capped chains (main equilibrium; Eq. 11), with only occasional termination by combination or disproportionation (Eqs. 12–13). This reversible transfer sequence repeatedly deactivates and reactivates the growing grafts, so that chains experience similar growth. Consequently, under our conditions, the M_w of the grafts is governed primarily by the monomer-to-RAFT ratio and conversion, while rapid the exchange suppresses premature termination, yielding reduced dispersity [30,31]. This explains how the RAFT agent controls side-chain growth of poly(VBC) on LDPE. Consequently, the first indication of this control is the degree of grafting (DoG) presented for samples, which were 220 %, 110 %, and 80 % for LG-0, LG-56, and LG-112, respectively.

I. Initiation

$$\text{Initiator} \rightarrow I^* \tag{7}$$

$$P + M \rightarrow P_m^* \tag{8}$$

II. Initial equilibrium

$$P_m^* \rightarrow \mathrm{RS(C = S)Z} \rightleftharpoons \mathrm{RS(C^* - S - Pm)Z} \rightleftharpoons \mathrm{PmS(C = S)Z} + R^* \tag{9}$$

III. *Reinitiation*

$$R^* + \mathrm{M} \xrightarrow{k_{re-in}} P_i^* \xrightarrow{M} \xrightarrow{k_p} P_n^* \tag{10}$$

IV. *Main equilibrium*

$$P_n^* + \mathrm{PmS(C=S)Z} \rightleftharpoons \mathrm{PmS(S-C^*-Pn)Z} \rightleftharpoons \mathrm{PnS(C=S)Z} + P_m^* \tag{11}$$

V. *Termination*

$$P_m^* + P_n^* \xrightarrow{k_\beta^c} P_{n+m} \tag{12}$$

or

$$P_m^* + P_n^* \xrightarrow{k_\beta^d} P_n^H + P_m^* \tag{13}$$

More specific to the system studied here, Scheme (SSc1) summarizes RIG polymerization of vinyl benzyl chloride onto LDPE by RAFT method to synthesize AEM.

Gel permeation chromatography (GPC) was used to investigate the molecular structure of non-RAFT (LG-0) and RAFT-based AEMs (LG-56 and LG-112). As shown in Fig. 2, the weight average molecular weight (M_w) decreases with increasing RAFT agent concentration. The calculated M_w values were 69,854, 12,024, and 7303 g mol^{-1} for LG-0, LG-56, and LG-112, respectively. A similar trend was observed for the dispersity index (Đ), which ranged from 4.9 (LG-0) to 1.7 (LG-56) and 1.6 (LG-112), indicating narrower molecular weight distributions in RAFT-AEMs compared to conventional RIG-AEMs. The distinct peak observed between 15 and 22.5 min confirms the effective graft copolymerization control by the RAFT agent, consistent with previous findings [32,33]. In addition, these results suggest that higher RAFT concentrations improve radical trapping, thus enabling precise polymerization control and the design of monodisperse polymers for targeted applications.

Raman spectroscopy was employed to confirm AEM synthesis and to characterize their molecular structure (Fig. 3). For LG-0, the spectra exhibited bands at 1447, 1293, 1130, and 1062 cm^{-1}, corresponding to CH_2 bending, CH_2 twisting, and C—C stretching modes, respectively, associated with the LDPE matrix [17,19], as observed by LDPE spectrum in Fig. 3. The structure of LDPE-*g*-poly(VBC) was evidenced by intense bands at 1610, 1220, and 1188 cm^{-1}, attributed to aromatic ring vibrations, CH_2–Cl groups, and C—C stretching from the LDPE backbone, respectively [19,34]. A comparative between the DoG vs. intensity of band at 1610 cm^{-1} is presented in Fig. S1, confirming the graft concentration difference for samples. Finaly, characteristics bands at 765 cm^{-1}, and 889 cm^{-1} (symmetrical stretching and asymmetric stretching, respectively), assigned to the trimethylammonium group, confirmed the success of the functionalization. Comparable Raman profiles were obtained for LG-56 and LG-112, indicating that grafting and amination proceeded effectively without pronouncing structural changes in the RAFT-based membranes. Although Çelik et al. [32] reported a band at 780 cm^{-1} attributed to the RAFT agent, no distinct vibration was observed at this position for LG-56 or LG-112. This absence is likely due to overlap with intense absorption bands from the grafted polymer in the same spectral region [32].

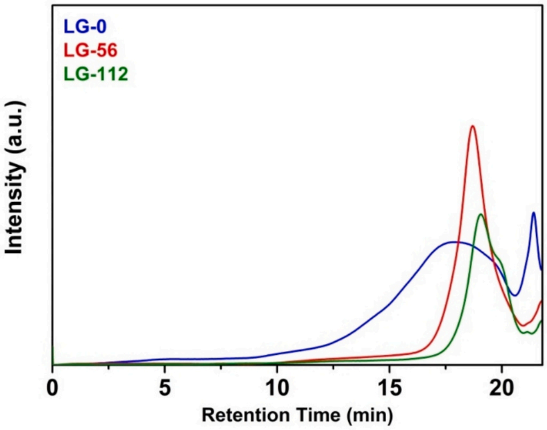

Fig. 2. GPC chromatograms of LG-0 (blue line), LG-56 (red line), and LG-112 (green line). (For interpretation of the references to color in this figure caption, the reader is referred to the Web version of this article). (For interpretation of the references to color in this figure legend, the reader is referred to the web version of this article.)

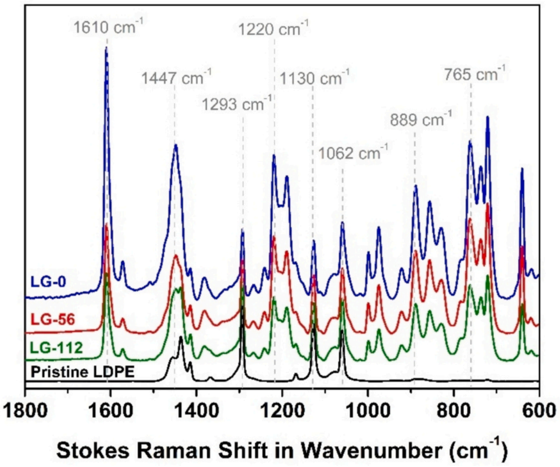

Fig. 3. Raman spectra for pristine LDPE (black line), and LG-0 (blue line), LG-56 (red line) and LG-112 (green line) AEMs. Spectra recorded with a laser of 785 nm. (For interpretation of the references to color in this figure caption, the reader is referred to the Web version of this article). (For interpretation of the references to color in this figure legend, the reader is referred to the web version of this article.)

Raman mapping was also employed to evaluate the distribution of VBC grafts across the cross-section of LDPE-grafted samples, aiming to assess the influence of the RAFT agent on graft distribution within the AEMs. Fig. 4 presents Raman cross-sectional maps obtained from the area ratio of the intensities at 1610 cm-1 (VBC aromatic ring) and 1130 cm-1 (C—C stretching), which depict the grafting levels at different regions throughout the membrane thickness. The Raman maps were not presented on the same intensity scale because the samples exhibit markedly different DoG values. Please see Fig. S4 for maps normalized to the same scale, which introduces visual artifacts, particularly for sample LG-0. Warm colors (red, yellow, and orange) indicate higher grafting concentration, whereas cold colors (blue, green, and purple) correspond to region with lower grafting concentration. For instance, Raman map of LG-0 reveals preferential grafting near the surfaces, as evidenced by the higher intensities at the extremities. Although the central region displays comparatively lower intensity values, the signal remains considerable, confirming that the grafting also occurred throughout the bulk, but with a more heterogeneous distribution. In contrast, RAFT-based samples (LG-56 and LG-112) displayed more uniform distributions: LG-56 showed a balanced profile with minor local variations, while LG-112 exhibited the most homogeneous distribution, suggesting that the RAFT agent enhances control over grafting and promotes uniformity across the membrane.

In addition to Raman cross-sectional maps, elemental mapping by EDS was carried out using chlorine as a marker of the VBC-grafted phase.

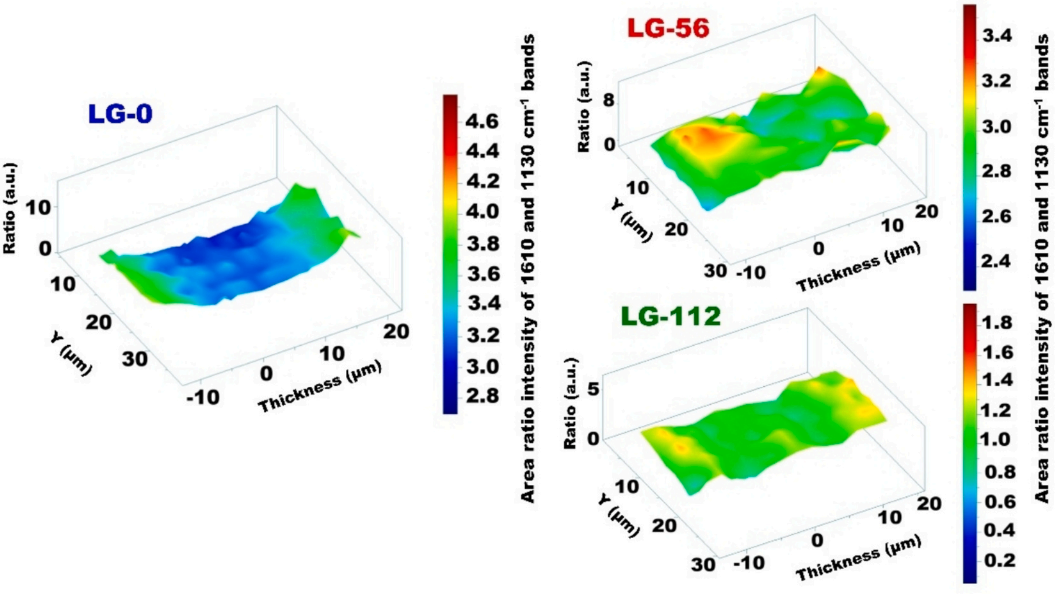

Fig. 4. Cross-sectional 3D-maps from the ratio between the integrated areas of the peaks 1610 cm^{-1}, related to the aromatic group of the monomer, and 1130 cm^{-1}, from the precursor LDPE film backbone.

The C/Cl superimposed maps (Fig. S2) revealed clear differences among the samples. For instance, LG-0 presented a dense and continuous distribution of chlorine across the thickness, with some local variations in terms of intensity, confirming bulk grafting despite its heterogeneity. On the other side, LG-56 displayed the most homogeneous distribution, with chlorine evenly dispersed across the cross-section, whereas LG-112 presented noticeable Cl$^-$deficient domains, suggesting less homogeneous grafting. These spatial trends are consistent with the IEC values (LG-0 ≈ LG-56 > LG-112) and reinforce the graft distribution differences inferred from Raman spectroscopy. While EDS does not provide absolute quantification in polymeric matrices, it reliably highlights relative chlorine distribution, serving as a complementary confirmation of the Raman data.

The evident difference in grafting homogeneity between the non-RAFT and RAFT-AEMs can be primarily attributed to the intrinsic nature of the grafting reaction. The grafting process is influenced by several factors, including solvent type, monomer concentration, diffusion kinetics, radical formation, and, in this case, the RIG protocol. These parameters strongly affect the grafting profile across the membrane cross-sectional [17,19]. Our previous studies demonstrated that the traditional RIG methodology based on simultaneous irradiation method provides more uniform graft distribution compared to the pre-irradiation method [14], but the pre-irradiation method can provide more homogenous graft distribution when the irradiation conditions as temperature, dose and atmosphere are controlled [17].

Among these factors, the dynamics of monomer diffusion within the polymer matrix require particular attention. Typically, diffusion initiates at the film surface, where polymer swelling facilitates penetration, and then proceeds along the concentration gradient toward the bulk. The solvent also plays a critical role taking into account that an inadequate solvent may hinder diffusion by raising the viscosity of the grafting solution due to poor solubility of the formed homopolymer. Considering that solvent, monomer concentration, irradiation dose, and RIG protocol was maintained unchanged for all AEMs. The differences observed in Fig. 4 can be entirely ascribed to the RAFT agent concentrations employed during RIG.

Beyond diffusion aspects, the RAFT agent has an important influence on graft uniformity by regulating polymerization kinetics. RAFT polymerization proceeds via a degenerative chain-transfer mechanism involving the chain transfer agent (CTA) and propagating radical. This mechanism provides fine control over polymerization by establishing a rapid equilibrium among growing chains, thus ensuring uniform extension [33]. The thiocarbonylthio-group and the R-group (leaving group) in the RAFT agent generate stable radicals upon cleavage, while the *Z*-group (stabilizing group) modulates reactivity, favoring controlled radical generation. This dynamic equilibrium promotes balanced chain propagation and uniform side-chain growth within the graft copolymer [33]. As a result, RIG-RAFT grafting produces films with narrower polymer size distributions, tailored by adjusting monomer and RAFT agent concentrations [29]. In contrast, conventional RIG approaches, although capable of achieving high grafting densities, lead to chains with disproportionate lengths. This explains why LG-0 exhibits poor graft homogeneity despite its high DoG, whereas the controlled chain growth mediated by the RAFT agent accounts for the improved graft uniformity in LG-56 and LG-112.

3.2. Physicochemical properties of AEMs

The RIG-RAFT method proved to be efficient in the synthesis of AEMs with well-defined architectures and controlled molecular weight distributions, providing suitable physicochemical and electrochemical properties for AEMFC application. Among these, parameters such as DoG, IEC, WU, IPS, and TPS data of non-RAFT (LG-0) and RAFT-AEMs (LG-56 and LG-112) are shown in Table 1.

Table 1
Summary of the fundamental properties of the non-RAFT and RAFT-AEMs: degree of grafting (DoG), ion exchange capacity (IEC), water uptake (WU), through plane swelling (TPS), and in-plane swelling (IPS).

AEMs	LG-0	LG-56	LG-112
DoG (%)	220 ± 1	110 ± 2	80 ± 1
IEC (mmol g^{-1})	3.1 ± 0.1	3.1 ± 0.1	1.6 ± 0.4
WU Cl$^-$ at 25 °C (%)	148 ± 5	150 ± 5	100 ± 6
WU OH$^-$ at 25 °C (%)	269 ± 2	258 ± 6	200 ± 4
WU OH$^-$ at 80 °C (%)	390 ± 8	385 ± 5	320 ± 5
IPS Cl$^-$ at 25 °C (%)	54 ± 5	55 ± 4	32 ± 2
TPS Cl$^-$ at 25 °C (%)	56 ± 2	52 ± 1	35 ± 3
Wet thickness (μm)*	72	70	57

* Thickness of AEMs in the hydroxide form at 25 °C.

In terms of DoG, it is possible to observe a decrease in DoG values when the amount of RAFT agent increases. In other words, under constant irradiation dose (25 kGy) and monomer concentration, increasing RAFT agent content leads to a significant reduction in DoG, from 220 % in LG-0 to 110 %, and 80 % for LG-56 and LG-112, respectively. These results indicate that the RAFT agent limits the grafting by controlling the polymerization reaction. In this scenario, a high RAFT agent concentration competes with each VBC monomer, thereby restricting poly (VBC) graft formation. A similar behavior was previously reported by our group for ETFE-based AEMs [16]. Furthermore, this effect can be also attributed to the capacity of the RAFT agent in regulating the molecular length of the side chains during the grafting process, taking into account that the RAFT agent binds to the monomer to mediate VBC graft copolymerization [16]. Therefore, this effect does not necessarily reflect a lower incorporation of VBC, but rather an increase in side-chain length, which may lead to an underestimation of the true DoG values determined gravimetrically.

The IEC values present no appreciable difference in IEC is observed between LG-0 and LG-56 AEMs (both 3.1 mmol g^{-1}), despite their DoG values of 220 % and 110 %, respectively. In contrast, LG-112 exhibits a significantly lower IEC of 1.6 mmol g^{-1}, which is unexpectedly low considering its DoG of 80 %. The IEC is indirectly related to the number of functional groups present, because chloride counterions are associated with the $-N(CH_3)_3^+$ groups introduced via VBC grafts. To corroborate this relationship and to rationalize the similar IEC values observed for LG-0 and LG-56 and the lower IEC for LG-112 (even though LG-56 and LG-112 exhibit relatively similar DoG, 110 % vs. 80 %), we correlated the integrated areas of the 765 and 889 cm^{-1} Raman bands, assigned to the symmetric and asymmetric stretching of the functional group, respectively, with IEC (Fig. 3). For example, the area of the 765 cm^{-1} band decreases progressively across LG-0 (74.6) > LG-56 (54.1) > LG-112 (35.1) (see Fig. S3). The same trend is observed for the 889 cm^{-1} band, supporting that the lower IEC of LG-112 arises from a reduced number of $-N(CH_3)_3^+$ groups. This reduction can be attributed to steric hindrance associated with the shorter side chains of the poly(VBC) grafts obtained under RAFT control. Consistently, GPC indicates a lower $\overline{M}_w$ for LG-112 (7303 g mol^{-1}), which may have limited the access of TMA during amination and led to the lower IEC. By contrast, LG-0 and LG-56 show same IEC values, even though the 765 cm^{-1} band area is clearly larger for LG-0, indicating a higher expected IEC. It is possible that the inconsistent organization of the poly(VBC) grafts in LG-0 also limited TMA accessibility due to steric hindrance effects, but further studies will be required to confirm this interpretation.

Water uptake (WU) is a critical parameter for ionomeric membranes in which water acts as the primary ion carrier in both Grøtthuss and vehicular mechanisms [35]. While higher WU enhances ion transport, it also reflects in dimensional parameters, such as in-plane (IPS) and through-plane swelling (TPS), which can impair mechanical integrity and electrode–membrane contact. Therefore, a balanced hydration that maximizes conductivity while preserving dimensional stability is essential for AEMFC durability [36–38].

As shown in Table 1, WU at 25 °C for AEMs in Cl^- form is similar for LG-0 (148 %) and LG-56 (150 %), and lower for LG-112 (100 %). This trend persists for AEMs in OH^- form (25 °C) with WU values of 269 % 258 % and 200 % for LG-0, LG-56, and LG-112, respectively. At 80 °C, WU increases to ~390 % for LG-0 and LG-56, and 320 % for LG-112. These differences correlate with IEC values (3.1 mmol g^{-1} for LG-0 and LG-56 vs. 1.6 mmol g^{-1} for LG-112), reinforcing that lower IEC in LG-112, associated to lower quantity of functional groups, constrains the water sorption.

Similarly to WU, IPS and TPS follow the same decreasing trend as the RAFT agent content increases. For AEMs in the Cl^- form at 25 °C, nearly identical expansion is observed for LG-0 (54 %, 56 %) and LG-56 (55 %, 52 %), whereas LG-112 shows lower expansion (32 %, 35 %). In the OH^- form, swelling becomes more pronounced at 80 °C, with IPS reaching 120 % (LG-0), 73 % (LG-56), and 48 % (LG-112). TPS follows the same trend. These results indicate that the more pronounced through-plane expansion at elevated temperature (80 °C, close to AEMFC operating conditions) observed for LG-0 and LG-56 may compromise the electrode–membrane interfacial contact and, consequently, the durability of the AEMFC. The temperature dependence of WU, IPS, and TPS in hydroxide form is presented in Fig. S4.

Finally, the wet thickness of the pristine LDPE film (25 μm) increased considerably, reaching ~70 μm for LG-0 and LG-56, and 57 μm for LG-112, as a result of the modifications introduced into the film (grafting and amination).

3.3. *Thermal properties*

To assess the thermal stability of the AEMs, TGA and DSC analyses were performed. Fig. 5 shows the TGA curves for pristine LDPE and AEMs (LG-0, LG-56, and LG-112). Pristine LDPE exhibits an abrupt mass loss at 450 °C due to depolymerization of C—H and C—C bonds, resulting in complete degradation. The AEMs display similar profiles with four thermal events: residual water evaporation (~60 °C), loss of TMA groups from poly(VBC)-based side chains (~200 °C), depolymerization of VBC groups attached to the LDPE backbone (~400 °C) [39], and LDPE backbone degradation at 450–500 °C [39,40].

Fig. S5 shows the DSC curves for pristine LDPE and AEMs (LG-0, LG-56, and LG-112). Pristine LDPE exhibits a melting temperature (Tm) peak at 115 °C and a crystallization temperature (Tc) peak at 96 °C. In contrast, all AEMs display a slight decrease in both Tm (~5 °C) and Tc (~10 °C) compared to pristine LDPE (see Table S2). The shift of the Tm and Tc peak to lower temperatures can indicate a reduction in crystallinity of samples. On the other hand, no appreciable changes were observed in Tm (110 °C for all samples) or Tc (84–88 °C) across the AEMs. Thus, the RAFT agent does not appear to directly influence these thermal characteristics.

The melting enthalpy (ΔH_m) of LDPE was determined by integrating the area under the melting peaks from onset to endset, allowing calculation of the degree of crystallinity (Xc) of the membranes. This calculation uses the ratio of the measured ΔH_m of each AEM to the theoretical heat of fusion for 100 % crystalline polyethylene ($\Delta H^\circ = 245.3$ J g^{-1}) [41,42]. The ΔH_m values followed the order: LG-0 < LG-56 < LG-112 < pristine LDPE (Table S2), indicating that the degree of crystallinity decreased substantially in all AEMs compared to pristine LDPE, irrespective of the grafting methodology. For example, Xc = 35 % for pristine LDPE vs 5 % for LG-0, 6 % for LG-56, and 7 % for LG-112.

3.4. *Mechanical properties*

Mechanical properties of solid polymeric electrolytes are crucial for AEMFC application once such properties are directly related to the stability and durability of the device [43–45]. Stress-strain curves are shown in Fig. 6 and corresponding parameters, such as elastic modulus (E_m), yield strength, elongation at break (E_b), and toughness, are summarized in Table 2. As shown, E_m values are relatively robust stiffness with LG-0 exhibiting 438 MPa, LG-56 = 500 MPa, and LG-112 = 691 MPa. Such feature indicates that the increase in RAFT agent content clearly enhances E_m, reflecting increased membrane rigidity. Interestingly, although an increase in molecular weight is typically associated with higher E_m values, the opposite trend was observed, i.e. the number-weight average molecular weight (M_w), as determined by GPC, decreases as RAFT content increases. Considering that LG-0 (with higher M_w) exhibits a higher degree of grafting compared to the RAFT-based AEMs, lower E_m can be related to increased graft content, which induces structural fragility in the polymer matrix.

Elongation at break (E_b) increases with RAFT content: LG-0 (154 %) < LG-56 (162 %) < LG-112 (200 %). As reported by Henkel & Vana [46], samples prepared without RAFT exhibit lower Eb than those synthesized via RAFT approach. Moreover, the trends in Em and Eb are consistent

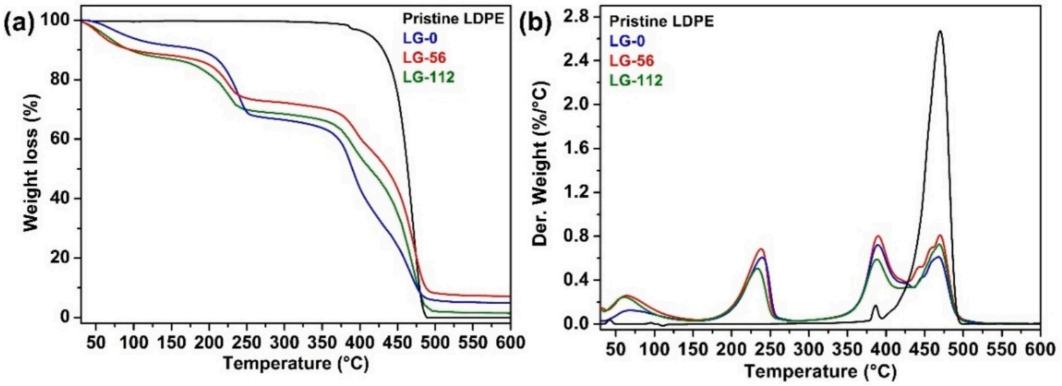

Fig. 5. TGA (a) and DTG (b) curves of membranes: LG-0 (blue line), LG-56 (red line), and LG-112 (green line). (For interpretation of the references to color in this figure caption, the reader is referred to the Web version of this article). (For interpretation of the references to color in this figure legend, the reader is referred to the web version of this article.)

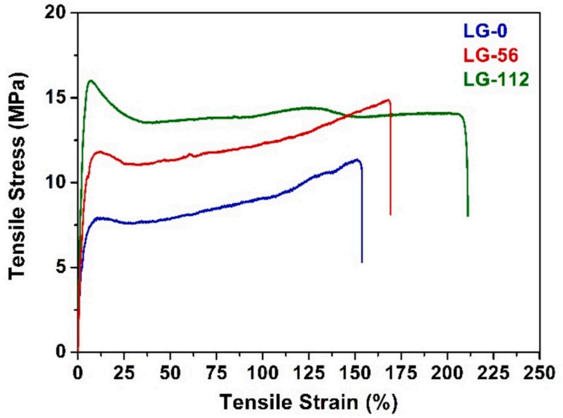

Fig. 6. Stress vs strain curves of AEMs LG-0 (blue line), LG-56 (red line), and LG-112 (green line) AEMs. (For color references in this figure caption, the reader is referred to the Web version of this article). (For interpretation of the references to color in this figure legend, the reader is referred to the web version of this article.)

Table 2
Mechanical properties of pristine LDPE, LG-0, LG-56 and LG-112 AEMs.

AEM	E_m (MPa)	Yield strength (MPa)	E_b (%)	Toughness (MJ m^{-3})
LG-0	438 ± 40	8 ± 2	154 ± 2	1342
LG-56	500 ± 25	12 ± 3	162 ± 5	2065
LG-112	691 ± 10	16 ± 2	200 ± 2	2945

with observations for ETFE-based AEMs prepared by the RAFT-RIG method [16], supporting our findings.

A similar trend is observed for yield strength, which increases progressively with RAFT agent content: LG-0 (8 MPa) < LG-56 (12 MPa) < LG-112 (16 MPa). Yield strength corresponds to the stress at which plastic deformation begins, thus serving as an indicator of the resistance of the polymer network to irreversible structural rearrangements. The gradual increase observed with RAFT incorporation suggests that the presence of RAFT-controlled grafting promotes a more uniform and compact network, enhancing the ability of the membranes to resist deformation under applied stress.

Toughness reflects the energy absorbed by the material before failure, integrating both strength and ductility into a single parameter. A pronounced increase in toughness with increasing RAFT content is also observed, with values of 1342 MJ m^{-3}, 2065 MJ m^{-3}, and 2945 MJ m^{-3} for LG-0, LG-56, and LG-112, respectively. The substantial increase in toughness with higher RAFT content indicates that these membranes not only withstand greater stresses but also exhibit enhanced capacity to dissipate mechanical energy during elongation, delaying catastrophic fracture. This synergistic enhancement underscores the advantage of RAFT-based AEMs simultaneously combining rigidity, strength, and ductility, which are critical parameters for mechanical robustness under operational stresses in AEMFC environments.

3.5. Morphological properties

AFM and SEM analyses were carried out to evaluate the influence of the RAFT agent on the surface morphology of the AEMs. Fig. 7a–f displays the surface images of the LG-0, LG-56, and LG-112 samples.

The AFM topographic profiles reveal pronounced differences among the membranes as presented in Fig. 7a–c. The AFM 3D maps are exhibited in Fig. S6. For instance, LG-0 sample shows a heterogeneous surface with the presence of distinct agglomerates and elevated domains. This irregular morphology results in a root mean square roughness (R_{rms}) value of 145 nm and reflects a non-uniform distribution of the grafted domains. Such behavior can be correlated with the high degree of grafting (DoG of 220 %) of this sample, suggesting that grafting occurred without spatial control, generating morphological heterogeneity. For LG-56 AEM, a slight increase in R_{rms} is observed (160 nm), accompanied by a redistribution of surface features that appear more elongated and continuous compared to LG-0. The formation of these structures indicates a surface reorganization process promoted by the addition of the RAFT agent, which contributes to a more uniform propagation of grafted chains. In contrast, the LG-112 sample exhibits a markedly smoother surface, with an R_{rms} of 70 nm, significantly lower than those of LG-0 and LG-56. This result indicates the development of a more homogeneous and compact surface, where the presence of agglomerates is considerably reduced, suggesting a higher degree of morphological stabilization.

The SEM images provide complementary evidence to the AFM findings (Fig. 7d–f). In LG-0, the surface is characterized by dispersed granules and irregular regions, compatible with the heterogeneous topography revealed by AFM. For LG-56, these granules are still observed, although they appear more evenly distributed, while the presence of grooves and oriented features is also consistent with the AFM observations. Finally, LG-112 exhibits a continuous and compact morphology, with a few visible agglomerates, confirming the reduction in roughness and the homogenization of the surface domains.

In general, these results demonstrate a morphological transition across the samples: from a rough and granular surface (LG-0) to a partially reorganized morphology (LG-56), culminating in a smooth and homogeneous structure in LG-112. This progressive structural evolution indicates that the introduction of the RAFT agent not only regulates the

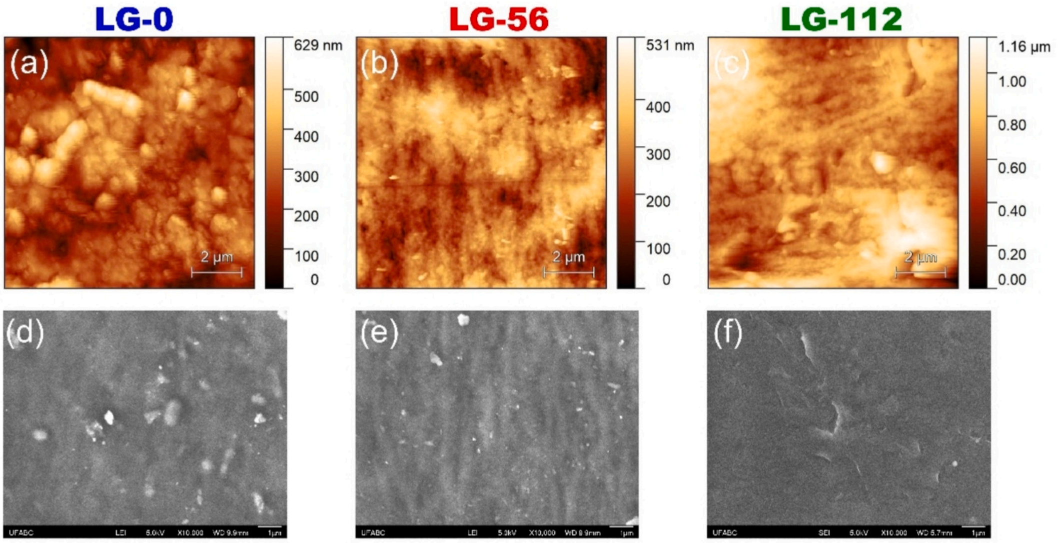

Fig. 7. AFM images with scale of 2 μm for AEMs (a-c), and SEM images with scale of 1 μm for AEMs.

molecular weight of the poly(VBC) grafts, but also plays an important role in controlling the spatial distribution of the grafted domains. Consequently, the RAFT-mediated process leads to AEMs with improved morphological uniformity, which may have direct implications for interfacial properties, stability, and overall electrochemical performance. In order to facilitate comparison of the microphase separated morphologies of membranes, it is possible to observe the images in Fig. S6.

3.6. OH^- conductivity

Fig. 8 shows the OH^- conductivity (σ) values of the AEM-series in the range of 30–80 °C, measured under CO_2-free conditions following the methodology described by Dekel et al. [25,26]. As expected, all AEMs exhibit Arrhenius-type behavior, indicating the thermally activated nature of OH^- transport. At 30 °C, the σ of LG-0, LG-56, and LG-112 were 115, 116, and 80 mS cm^{-1}, respectively, while at 80 °C the conductivities increased to 228, 230, and 153 mS cm^{-1}. These results demonstrate that LG-0 and LG-56 present nearly identical conductivities throughout the entire temperature range, whereas LG-112 consistently exhibits significantly lower values.

The σ trends are consistent with the structural and hydration properties discussed earlier. LG-0 and LG-56 combine a relatively high IEC (~3 mmol g^{-1}) with substantial water uptake (~150 %), enabling the formation of interconnected hydrated domains that favor both vehicular and Grøtthuss-type transport mechanisms [47–49]. In contrast, although LG-112 maintains a considerable WU (~100 %), its IEC is nearly half that of LG-0 and LG-56 (~1.6 mmol g^{-1}), limiting the density of quaternary ammonium groups and reducing the continuity of OH^- transport pathways, which explains its lower conductivity values.

The activation energies (Ea) extracted from the Arrhenius plots further support these findings. The Ea values were 11.3, 11.6, and 10.8 kJ mol^{-1} for LG-0, LG-56, and LG-112, respectively. These relatively low and similar values indicate that OH^- transport in all AEMs is governed by comparable mechanisms, with only minor differences in the energetic barrier. The lower Ea for LG-112 suggests that its ion transport is not hindered by higher energetic requirements, but by the reduced number of available conduction sites due to its lower IEC.

A brief comparison reveals a clear balance between hydration, IEC, and conductivity, in which LG-0 and LG-56 provide superior OH^- conduction but with higher dimensional swelling, whereas LG-112 offers reduced swelling due to lower ion transport efficiency.

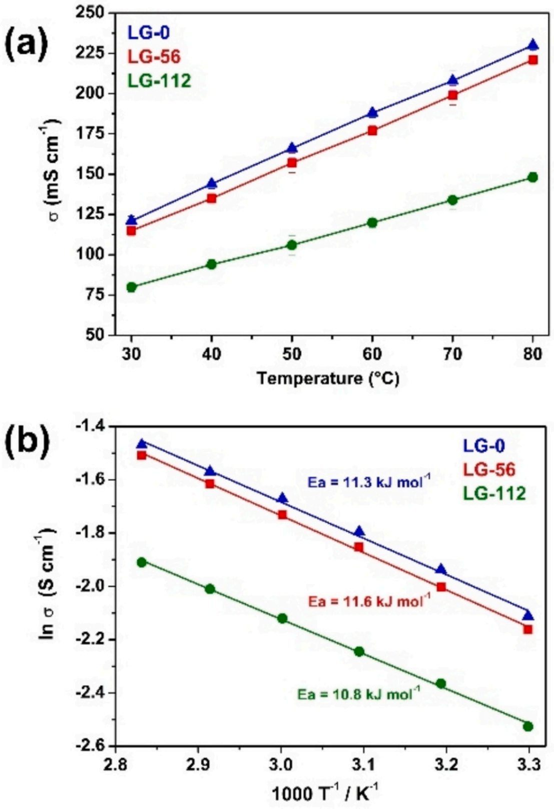

Fig. 8. Temperature dependence of the ionic conductivity at RH = 100 %, measuring the "*true hydroxide conductivity*" (a), and Arrhenius-plot (b). (For interpretation of the references to color in this figure caption, the reader is referred to the Web version of this article).

3.7. Alkaline stability of membranes

The chemical stability of AEMs was evaluated using an alkaline degradation test, in which the membranes were immersed in 1 M KOH solution at 80 °C for 720 h. Stability was assessed in terms of IEC loss, calculated as the difference before and after the test.

The IEC loss data are summarized in Fig. 9a. After the alkaline

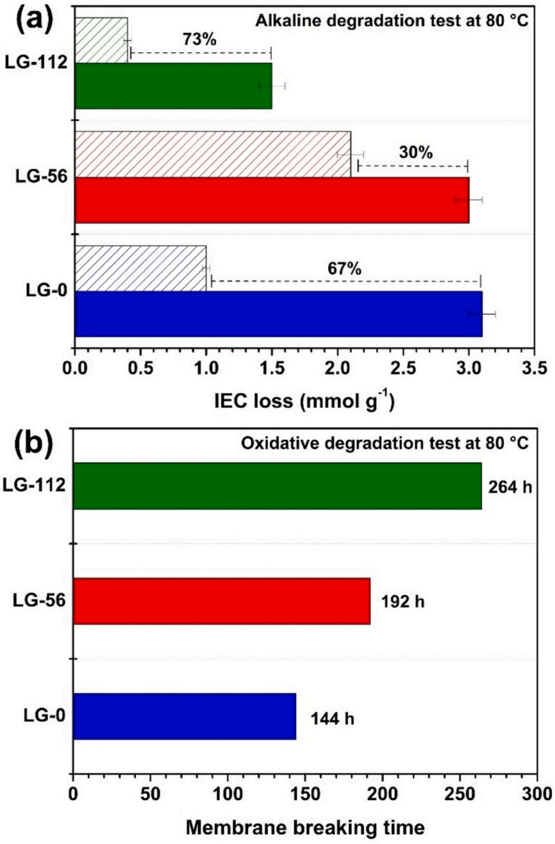

Fig. 9. The initial and final IEC for membranes obtained in alkaline degradation test using KOH (1 M) solution at 80 °C after 720 h (a). The oxidative degradation test at 80 °C using Fenton reagent (b). (For interpretation of the references to color in this figure caption, the reader is referred to the Web version of this article).

degradation test, both LG-0 and LG-112 exhibited severe losses of approximately 70 %, while LG-56 showed a lower IEC loss of only 30 %. These results highlight the improved alkaline stability of the RAFT-based LG-56 membrane compared to both non-RAFT and high-RAFT-content AEMs. The reduced loss in LG-56 can be explained by the structural control introduced by the RAFT agent, which provides better chain regulation and seems to mitigate the degradation. This interpretation is consistent with the cross-sectional Raman mapping results, which revealed a good homogeneous graft distribution, and with AFM/SEM analyses, which showed surface modifications indicative of more controlled morphologies for LG-56 AEMs.

In all cases, the chemical degradation is primarily associated with the cleavage of QA groups, which represent the functional sites responsible for ion transport. The dominant pathway is nucleophilic substitution (S_N2), in which hydroxide ions attack the benzylic carbon, leading to the detachment of the trimethylammonium moiety and the concomitant formation of benzyl alcohol [40,50,51]. This reaction results in a permanent loss of ionic sites, directly reducing the IEC. Additional degradation routes also contribute to the chemical instability of AEMs. Hofmann elimination, for instance, occurs when hydroxide abstracts a β-hydrogen, producing an alkene and a tertiary amine, which is non-conductive. Furthermore, hydroxide can induce demethylation of QA groups, generating dimethylamine derivatives that are less stable, or attack the α-hydrogen of the methylene group, leading to tertiary amine formation and further disrupting ion transport [40,50,51]. Consequently, these pathways progressively decrease the density of functional groups, alter the hydrophilic–hydrophobic balance of the polymer, and compromise both conductivity and mechanical integrity. The extent to which each pathway dominates can vary depending on molecular architecture, molecular weight, local environment, and the accessibility of QA groups, highlighting the critical role of structural control imparted by RAFT in mitigating such degradation [16,52–55].

Oxidative stability test was also evaluated using the Fenton reagent at 80 °C. The membranes were kept under these conditions until rupture, and the breaking time was empirically identified. As shown in Fig. 9b, the break occurred after 164 h for LG-0, 192 h for LG-56, and 264 h for LG-112. These results are consistent with the mechanical properties discussed earlier, confirming that oxidative attack weakens the polymer backbone and increases brittleness. Although the degradation mechanisms in alkaline and oxidative conditions are fundamentally different. Both sets of results demonstrate that RAFT incorporation enhances the stability of AEMs. The oxidative degradation test simulates radical attack conditions that can occur during fuel cell operation due to peroxide intermediates. In the Fenton system, hydroxyl (•OH) and hydroperoxyl (•OOH) radicals generated from H_2O_2 decomposition can abstract hydrogens from the polymer backbone, initiating chain scission and structural weakening [56,57]. This process gradually reduces mechanical integrity, leading to embrittlement and eventual rupture, as shown in Fig. 9b. While LG-56 and LG-112 exhibited longer breaking times than LG-0, their different behaviors suggest that graft distribution and molecular organization influence how radicals propagate through the material. See the breaking of LG-112 AEM after degradation teste in Fig. S7. These results demonstrate that RAFT-mediated structural control enhances not only alkaline but also oxidative stability.

Summarily, these findings indicate that the improved stability of RAFT-based AEMs arises from the well-defined molecular architecture achieved by controlled chain growth, which generates steric hindrance, mitigates hydroxide attack, and promotes more uniform morphologies. In particular, LG-56 exemplifies the balance between controlled grafting and structural organization, as evidenced by Raman, AFM, and SEM results, ultimately leading to superior chemical durability.

3.8. *AEMFC results*

One of the aims of this work was to provide evidence for understanding how molecular weight control influences the physicochemical and electrochemical properties of AEMs in fuel cells. For that, the resulting AEMs were tested as polymeric electrolyte in single AEMFC at 80 °C. The polarization curves and respective power density curves for LG-0, LG-56, and LG-112 are shown in Fig. 10. All membranes exhibit a typical AEMFC polarization profile, characterized by activation, ohmic, and mass transport overpotentials with notable differences observed in the ohmic and diffusional regions. It is important to mention that both ohmic resistance and diffusion processes are water dependent. In the ohmic region, water is directly related to ionic transport processes, which impact OH^- conductivity. On the other hand, the mass transport limitation overpotential is strongly influenced by water imbalance at the anode and cathode interfaces, impairing the reactant gas diffusion.

In terms of performance, LG-0 and LG-56 AEMs exhibited the same maximum power density of approximately 1.3 W cm^{-2} at 2.7 A cm^{-2}, while LG-112 AEM reached a lower peak power density of 0.9 W cm^{-2} at 1.7 A cm^{-2}. This difference is attributed to variations in both ohmic and diffusion resistances in the LG-112 sample, as evidenced by a lower slope at intermediate current densities and a shift of the limiting current toward higher current densities.

Although LG-0 and LG-56 have significantly different M_w (69,854 and 12,024 g mol^{-1}, respectively), they exhibit similar IEC values and performance. In contrast, LG 112 has a M_w closer to that of LG-56 (7303 g mol^{-1}). but presents a markedly lower IEC and poor performance. These observations suggest that IEC is the dominant factor influencing performance in beginning-of-life experiments. On the other hand, AEMFC durability is a key factor and relies on the stability of the membrane–electrode assembly, particularly the AEM.

Fig. 10b shows the AEMFC short-term durability tests operating at

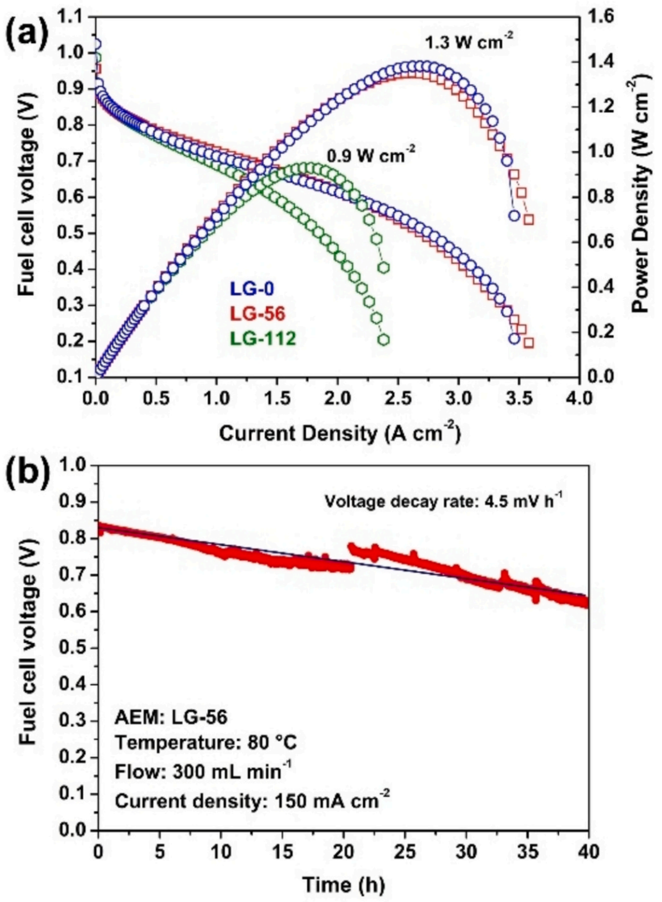

Fig. 10. AEMFCs performances at 80 °C with H_2 anode gas flow = 1.0 L min^{-1}, O_2 cathode gas flow = 1.0 L min^{-1}, both supplied unpressurised with optimal dew-point temperature of 77 °C (a). The short-term durability for LG-56 AEM at a constant current density of 150 mA cm^{-2}, 80 °C, 300 mL min^{-1}, and RH = 100 % (b). (For interpretation of the references to color in this figure caption, the reader is referred to the Web version of this article).

80 °C. The results showed that AEMFCs assembled from LG-56 AEM had a voltage decay rate of 4.5 mV h^{-1} (at a constant current density of 150 mA cm^{-2}) after 40 h. It is important to consider that durability performance in single fuel cell does not reflect the AEM degradation, but several contributing factors, including electrocatalysts stability, ionomer degradation, water management and the intrinsic properties of the AEM.

A direct correlation between performance parameters and chemical and mechanical stability shows that LG-56 maintains a power density comparable to that of LG-0 while reducing the IEC loss from 67 % to 30 %, thereby significantly improving alkaline stability. This suggests that controlling the molecular structure of AEMs through an intermediate amount of RAFT agent, as in LG-56, can enhance chemical and mechanical stability, without compromising key properties related to anion conduction that is essential for achieving high performance in AEMFCs.

4. Conclusions

We prepared a series of AEMs using a RAFT agent in conjunction with the radiation-induced grafting method to tailor the grafted molecular structure, aiming to achieve high AEMFC performance and good stability. Control over the grafted molecular structure was evidenced by the reduction in the degree of grafting and the narrowing of the peak in the GPC curves as the RAFT agent concentration increased, leading to the synthesis of AEMs with well-controlled molecular weight. Consequently, samples prepared with our RIG-RAFT protocol exhibited improved homogeneity in graft distribution, while the AEM prepared by traditional RIG exhibited lower graft distribution in bulk, as verified by cross-sectional Raman microscopy. These factors contributed to enhanced mechanical properties for RAFT-AEMs, thereby providing good mechanical stability. Furthermore, high IEC and OH$^-$ conductivity was achieved in RAFT-AEMs without compromising their water absorption and mechanical properties. AFM images revealed an irregular surface for the non-RAFT sample, with a high R_{rms} (148 nm), which was attributed to the non-uniformity of the grafts. On the other hand, the RAFT samples presented a significant visual change on the surface, suggesting a more organized surface attributed to effective control of the graft molecular weight. Consistently, AEMFC results showed that RAFT-AEMs delivered fuel cell performance comparable to that of non-RAFT AEMs (~1.3 W cm^{-2}), while demonstrating superior alkaline stability (67 % IEC loss for non-RAFT AEMs vs. 30 % for RAFT-AEMs). Overall, RAFT-AEMs are well-tailored, exhibit suitable mechanical and alkaline stability, enhanced surface morphology, and deliver high AEMFC performance, making them promising candidates for fuel cell applications.

CRediT authorship contribution statement

Yasko Kodama: Writing – review & editing, Writing – original draft, Visualization, Methodology, Investigation, Data curation, Conceptualization. **Andrey S. Barbosa:** Writing – review & editing, Writing – original draft, Visualization, Methodology, Investigation, Data curation, Conceptualization. **Bianca P.S. Santos:** Writing – original draft, Methodology, Investigation, Data curation. **Marcelo Linardi:** Writing – review & editing, Resources, Project administration. **Elisabete I. Santiago:** Writing – review & editing, Writing – original draft, Supervision, Resources, Project administration, Funding acquisition, Conceptualization.

Declaration of competing interest

The authors declare that they have no known competing financial interests or personal relationships that could have appeared to influence the work reported in this paper.

Acknowledgments

The authors acknowledge the support from FAPESP (grant no. 2017/11987-4, grant no. 2017/11937-4) and Shell and the strategic importance of the support provided by ANP (Brazil's National Oil, Natural Gas, and Biofuels Agency). The authors are thanks to the funding support of CNPq IBH2-MCTI No. 405793/2022-7, CNPq SisH2 No. 407967/2022-2, FAPESP by projects no. 2022/07786-9, 2023/14931-8, and 2024/01763-2. The authors acknowledge financial support from the International Atomic Energy Agency, research project contract: IAEA RC 23708. In addition, we thank the support given by the Radiation Technology Center at IPEN/CNEN for providing the facilities for the conduction of experiments and data analysis. The XploRA-PLUS was financially supported by Financiadora de Estudos e Projetos (Finep) – Grant: 01.18.0073.00. EIS is research fellows of the Brazilian CNPq.

Appendix A. Supplementary data

Supplementary data to this article can be found online at https://doi.org/10.1016/j.reactfunctpolym.2025.106526.

Data availability

Data will be made available on request.

References

[1] R. Espiritu, M. Mamlouk, K. Scott, Study on the effect of the degree of grafting on the performance of polyethylene-based anion exchange membrane for fuel cell application, Int. J. Hydrogen Energy 41 (2016) 1120–1133, https://doi.org/10.1016/j.ijhydene.2015.10.108.

[2] W. You, K.J.T. Noonan, G.W. Coates, Alkaline-stable anion exchange membranes: a review of synthetic approaches, Prog. Polym. Sci. 100 (2020) 101177, https://doi.org/10.1016/j.progpolymsci.2019.101177.

[3] J.O. Zoppe, N.C. Ataman, P. Mocny, J. Wang, J. Moraes, H.A. Klok, Surface-initiated controlled radical polymerization: state-of-the-art, opportunities, and challenges in surface and Interface engineering with polymer brushes, Chem. Rev. 117 (2017) 1105–1318, https://doi.org/10.1021/acs.chemrev.6b00314.

[4] Z.F. Pan, L. An, T.S. Zhao, Z.K. Tang, Advances and challenges in alkaline anion exchange membrane fuel cells, Prog. Energy Combust. Sci. 66 (2018) 141–175, https://doi.org/10.1016/j.pecs.2018.01.001.

[5] L. Gubler, Polymer design strategies for radiation-grafted fuel cell membranes, Adv. Energy Mater. 4 (2014) 1300827, https://doi.org/10.1002/aenm.201300827.

[6] S. Gottesfeld, D.R. Dekel, M. Page, C. Bae, Y. Yan, P. Zelenay, Y.S. Kim, Anion exchange membrane fuel cells: current status and remaining challenges, J. Power Sources 375 (2018) 170–184, https://doi.org/10.1016/j.jpowsour.2017.08.010.

[7] M. Mamlouk, J.A. Horsfall, C. Williams, K. Scott, Radiation grafted membranes for superior anion exchange polymer membrane fuel cells performance, Int. J. Hydrogen Energy 37 (2012) 11912–11920, https://doi.org/10.1016/j.ijhydene.2012.05.117.

[8] Mrinmay Mandal, Garrett Huang, Noor Ul Hassan, Xiong Peng, Taoli Gu, Ahmon H. Brooks-Starks, Bamdad Bahar, William E. Mustain, Paul A. Kohl, The importance of water transport in high conductivity and high-power alkaline fuel cells, J. Electrochem. Soc. 167 (2020), https://doi.org/10.1149/2.0022005JES.

[9] R. Gutru, Z. Turtayeva, F. Xu, G. Maranzana, B. Vigolo, A. Desforges, A comprehensive review on water management strategies and developments in anion exchange membrane fuel cells, Int. J. Hydrogen Energy 45 (2020) 19642–19663, https://doi.org/10.1016/j.ijhydene.2020.05.026.

[10] K. Yassin, I.G. Rasin, S. Brandon, D.R. Dekel, Quantifying the critical effect of water diffusivity in anion exchange membranes for fuel cell applications, J. Memb. Sci. 608 (2020) 118206, https://doi.org/10.1016/j.memsci.2020.118206.

[11] E.I. Santiago, J.J. Linares, Smart electrolytes: materials, durability, and degradation issues, in: M. Lo Faro, S.C. Zignani (Eds.), Polymer Electrolyte-based Electrochemical Devices, 2024, pp. 91–141, https://doi.org/10.1016/B978-0-323-89784-6.00003-6.

[12] J.R. Varcoe, P. Atanassov, D.R. Dekel, A.M. Herring, M.A. Hickner, P.A. Kohl, A. R. Kucernak, W.E. Mustain, K. Nijmeijer, K. Scott, T. Xu, L. Zhuang, Anion-exchange membranes in electrochemical energy systems, Energ. Environ. Sci. 7 (2014) 3135–3191, https://doi.org/10.1039/c4ee01303d.

[13] A. Brouzgou, A. Podias, P. Tsiakaras, PEMFCs and AEMFCs directly fed with ethanol: a current status comparative review, J. Appl. Electrochem. 43 (2013) 119–136, https://doi.org/10.1007/s10800-012-0513-2.

[14] A.L.G. Biancolli, A.S. Barbosa, Y. Kodama, R.R. de Sousa, A.J.C. Lanfredi, F. C. Fonseca, J.F.Q. Rey, E.I. Santiago, Unveiling the influence of radiation-induced grafting methods on the properties of polyethylene-based anion-exchange membranes for alkaline fuel cells, J. Power Sources 512 (2021), https://doi.org/10.1016/j.jpowsour.2021.230484.

[15] A.L.G. Biancolli, S. Bsoul-Haj, J.C. Douglin, A.S. Barbosa, R.R. de Sousa, O. Rodrigues, A.J.C. Lanfredi, D.R. Dekel, E.I. Santiago, High-performance radiation grafted anion-exchange membranes for fuel cell applications: effects of irradiation conditions on ETFE-based membranes properties, J. Memb. Sci. 641 (2022), https://doi.org/10.1016/j.memsci.2021.119879.

[16] B.P.S. Santos, A.S. Barbosa, Y. Kodama, T.B. de Queiroz, E.I. Santiago, Tailoring highly stable anion exchange membranes with graft molecular structure ordering using reversible addition-fragmentation chain transfer polymerization for alkaline fuel cells, J. Memb. Sci. 687 (2023) 122071, https://doi.org/10.1016/j.memsci.2023.122071.

[17] A.S. Barbosa, A.L.G. Biancolli, A.J.C. Biancolli, O. Lanfredi, F.C. Rodrigues, E.I. Santiago Fonseca, Enhancing the durability and performance of radiation-induced grafted low-density polyethylene-based anion-exchange membranes by controlling irradiation conditions, J. Memb. Sci. 659 (2022), https://doi.org/10.1016/j.memsci.2022.120804.

[18] L. Wang, X. Peng, W.E. Mustain, J.R. Varcoe, Radiation-grafted anion-exchange membranes: the switch from low- to high-density polyethylene leads to remarkably enhanced fuel cell performance, Energ. Environ. Sci. 12 (2019) 1575–1579, https://doi.org/10.1039/c9ee00331b.

[19] L. Wang, J.J. Brink, Y. Liu, A.M. Herring, J. Ponce-González, D.K. Whelligan, J. R. Varcoe, Non-fluorinated pre-irradiation-grafted (peroxidated) LDPE-based anion-exchange membranes with high performance and stability, Energ. Environ. Sci. 10 (2017) 2154–2167, https://doi.org/10.1039/c7ee02053h.

[20] G. Couture, B. Améduri, Kinetics of RAFT homopolymerisation of vinylbenzyl chloride in the presence of xanthate or trithiocarbonate, Eur. Polym. J. 48 (2012) 1348–1356, https://doi.org/10.1016/j.eurpolymj.2012.03.020.

[21] J.C. Foster, S.C. Radzinski, J.B. Matson, Graft polymer synthesis by RAFT transfer-to, J. Polym. Sci. A 55 (2017) 2865–2876, https://doi.org/10.1002/pola.28621.

[22] M. Barsbay, Y. Kodama, O. Güven, Functionalization of cellulose with epoxy groups via γ-initiated RAFT-mediated grafting of glycidyl methacrylate, Cellulose 21 (2014) 4067–4079, https://doi.org/10.1007/s10570-014-0416-y.

[23] L. Wang, E. Magliocca, E.L. Cunningham, W.E. Mustain, S.D. Poynton, R. Escudero-Cid, M.M. Nasef, J. Ponce-González, R. Bance-Souahli, R.C.T. Slade, D. K. Whelligan, J.R. Varcoe, An optimised synthesis of high performance radiation-grafted anion-exchange membranes, Green Chem. 19 (2017) 831–843, https://doi.org/10.1039/c6gc02526a.

[24] M. Shirazi, G.M. Rad, Y. Tamsilian, Polymer nanocomposite characterization and applications, Encycl. Mater. Compos. 1 (2021) 725–745, https://doi.org/10.1016/B978-0-12-819724-0.00083-5.

[25] N. Ziv, D.R. Dekel, A practical method for measuring the true hydroxide conductivity of anion exchange membranes, Electrochem. Commun. 88 (2018) 109–113, https://doi.org/10.1016/j.elecom.2018.01.021.

[26] A. Zhegur-Khais, F. Kubannek, U. Krewer, D.R. Dekel, Measuring the true hydroxide conductivity of anion exchange membranes, J. Memb. Sci. 612 (2020) 118461, https://doi.org/10.1016/j.memsci.2020.118461.

[27] Y. Wu, J. Song, T. Zhao, Y. Xie, D. Liu, L. Wang, G. Wei, H. Ma, Z. Wang, Polycarbazole-based anion exchange membranes containing flexible side-chain linked piperidine pendants for alkaline fuel cells, J. Memb. Sci. 707 (2024), https://doi.org/10.1016/j.memsci.2024.123031.

[28] M.M. Nasef, Radiation grafted ion conducting membranes for electrochemical energy systems: status of developmental and upscaled membranes, J. Appl. Membr. Sci. Technol. 26 (2022) 51–76, https://doi.org/10.11113/amst.v26n1.233.

[29] G. Moad, E. Rizzardo, S.H. Thang, Living radical polymerization by the RAFT process a second update, Aust. J. Chem. 62 (2009) 1402–1472, https://doi.org/10.1071/CH09311.

[30] G. Moad, Y.K. Chong, R. Mulder, E. Rizzardo, S.H. Thang, New features of the mechanism of RAFT polymerization, ACS Symp. Ser. 1024 (2009) 3–18, https://doi.org/10.1021/bk-2009-1024.ch001.

[31] M. Semsarilar, S. Perrier, “Green” reversible addition-fragmentation chain-transfer (RAFT) polymerization, Nat. Chem. 2 (2010) 811–820, https://doi.org/10.1038/nchem.853.

[32] G. Çelik, M. Barsbay, O. Güven, Towards new proton exchange membrane materials with enhanced performance via RAFT, Polym. Chem. (2015), https://doi.org/10.1039/c5py01527h.

[33] J. Chen, N. Seko, Effects of RAFT agent on the chloromethylstyrene polymerizations in a simultaneous radiation grafting system, Polymers (Basel) 9 (2017), https://doi.org/10.3390/polym9080307.

[34] K.M. Meek, C.M. Reed, B. Pivovar, K.D. Kreuer, J.R. Varcoe, R. Bance-Soualhi, The alkali degradation of LDPE-based radiation-grafted anion-exchange membranes studied using different ex situ methods, RSC Adv. 10 (2020) 36467–36477, https://doi.org/10.1039/d0ra06484j.

[35] D. Dong, W. Zhang, A.C.T. Van Duin, D. Bedrov, Grotthuss versus vehicular transport of hydroxide in anion-exchange membranes: insight from combined reactive and nonreactive molecular simulations, J. Phys. Chem. Lett. 9 (2018) 825–829, https://doi.org/10.1021/acs.jpclett.8b00004.

[36] C.E. Diesendruck, D.R. Dekel, Water – a key parameter in the stability of anion exchange membrane fuel cells, Curr. Opin. Electrochem. 9 (2018) 173–178, https://doi.org/10.1016/j.coelec.2018.03.019.

[37] Q. Ge, X. Zhu, Z. Yang, Highly conductive and water-swelling resistant anion exchange membrane for alkaline fuel cells, Int. J. Mol. Sci. 20 (2019), https://doi.org/10.3390/ijms20143470.

[38] M. Van Truong, N.B. Duong, C.L. Wang, H. Yang, Effects of cell temperature and reactant humidification on anion exchange membrane fuel cells, Materials 12 (2019), https://doi.org/10.3390/ma12132048.

[39] J. Ponce-González, D.K. Whelligan, L. Wang, R. Bance-Soualhi, Y. Wang, Y. Peng, H. Peng, D.C. Apperley, H.N. Sarode, T.P. Pandey, A.G. Divekar, S. Seifert, A. M. Herring, L. Zhuang, J.R. Varcoe, High performance aliphatic-heterocyclic benzyl-quaternary ammonium radiation-grafted anion-exchange membranes, Energ. Environ. Sci. 9 (2016) 3724–3735, https://doi.org/10.1039/c6ee01958g.

[40] A.S. Barbosa, A.L.G. Biancolli, B.P.S. Santos, J.J. Bonvent, D. Hermida-Merino, E. I. Santiago, Advancements in radiation-induced grafted anion-exchange membranes: controlling pre-irradiation parameters of high-density polyethylene for enhanced fuel cell performance and durability, React. Funct. Polym. 208 (2025), https://doi.org/10.1016/j.reactfunctpolym.2025.106149.

[41] D. Li, L. Zhou, X. Wang, L. He, X. Yang, Effect of crystallinity of polyethylene with different densities on breakdown strength and conductance property, Materials 12 (2019), https://doi.org/10.3390/ma12111746.

[42] Y.J. Choi, M.S. Kang, J. Cho, S.H. Moon, Preparation and characterization of LDPE/polyvinylbenzyl trimethyl ammonium salts anion-exchange membrane, J. Memb. Sci. 221 (2003) 219–231, https://doi.org/10.1016/S0376-7388(03)00265-5.

[43] M.A. Vandiver, B.R. Caire, T.P. Pandey, Y. Li, S. Seifert, A. Kusoglu, D.M. Knauss, A.M. Herring, M.W. Liberatore, Effect of hydration on the mechanical properties and ion conduction in a polyethylene-b-poly(vinylbenzyl trimethylammonium) anion exchange membrane, J. Memb. Sci. 497 (2016) 67–76, https://doi.org/10.1016/j.memsci.2015.09.034.

[44] R. Gutru, Z. Turtayeva, F. Xu, B. Vigolo, A. Desforges, I.J. Lamour, A comprehensive review on water management strategies and developments in anion exchange membrane fuel cells, ScienceDirect 5 (2020), https://doi.org/10.1016/j.ijhydene.2020.05.026.

[45] W.E. Mustain, Understanding how high-performance anion exchange membrane fuel cells were achieved: component, interfacial, and cell-level factors, Curr. Opin. Electrochem. 12 (2018) 233–239, https://doi.org/10.1016/j.coelec.2018.11.010.

[46] R. Henkel, P. Vana, The influence of RAFT on the microstructure and the mechanical properties of photopolymerized poly(butyl acrylate) networks, Macromol. Chem. Phys. 215 (2014) 182–189, https://doi.org/10.1002/macp.201300581.

[47] D.R. Dekel, M. Amar, S. Willdorf, M. Kosa, S. Dhara, C.E. Diesendruck, Effect of water on the stability of quaternary ammonium groups for anion exchange

membrane fuel cell applications, Chem. Mater. 29 (2017) 4425–4431, https://doi.org/10.1021/acs.chemmater.7b00958.

[48] A.M. Ahmed Mahmoud, K. Miyatake, Highly conductive and alkaline stable partially fluorinated anion exchange membranes for alkaline fuel cells: effect of ammonium head groups, J. Memb. Sci. 643 (2022) 120072, https://doi.org/10.1016/j.memsci.2021.120072.

[49] H. Koshikawa, K. Yoshimura, W. Sinnananchi, T. Yamaki, M. Asano, K. Yamamoto, S. Yamaguchi, H. Tanaka, Y. Maekawa, Counter-anion effect on the properties of anion-conducting polymer electrolyte membranes prepared by radiation-induced graft polymerization, Macromol. Chem. Phys. 214 (2013) 1756–1762, https://doi.org/10.1002/macp.201300225.

[50] R. Espiritu, B.T. Golding, K. Scott, M. Mamlouk, Degradation of radiation grafted anion exchange membranes tethered with different amine functional groups via removal of vinylbenzyl trimethylammonium hydroxide, J. Power Sources 375 (2018) 373–386, https://doi.org/10.1016/j.jpowsour.2017.07.074.

[51] R. Espiritu, B.T. Golding, K. Scott, M. Mamlouk, Degradation of radiation grafted hydroxide anion exchange membrane immersed in neutral pH: removal of vinylbenzyl trimethylammonium hydroxide due to oxidation, J Mater Chem A 5 (2017) 1248–1267, https://doi.org/10.1039/c6ta08232g.

[52] J. Han, J. Pan, C. Chen, L. Wei, Y. Wang, Q. Pan, N. Zhao, B. Xie, L. Xiao, J. Lu, L. Zhuang, Effect of micromorphology on alkaline polymer electrolyte stability, ACS Appl. Mater. Interfaces 11 (2019) 469–477, https://doi.org/10.1021/acsami.8b09481.

[53] H. Long, B.S. Pivovar, Hydroxide degradation pathways for substituted benzyltrimethyl ammonium: a DFT study, ECS Electrochem. Lett. 4 (2015) F13–F16, https://doi.org/10.1149/2.0041501eel.

[54] Q. Ge, G. Wang, X. Zhu, W. Yu, J. Zhou, B. Wu, Y. Liu, Z. Zheng, Z. Yang, J. Qian, A highly stable aliphatic backbone from visible light-induced RAFT polymerization for anion exchange membranes, Polym. Chem. 12 (2021) 5574–5582, https://doi.org/10.1039/d1py00867f.

[55] Q. Ge, G. Li, W. Jiang, X. Dong, X. Duan, B. Wu, J. Miao, S. Tao, Z. Yang, R. Fu, J. Qian, Constructing lamellar micromorphology in fluorinated, block anion exchange membranes from photocontrolled RAFT polymerization, J. Power Sources 624 (2024), https://doi.org/10.1016/j.jpowsour.2024.235559.

[56] Z. Feng, G. Gupta, M. Mamlouk, Degradation of QPPO-based anion polymer electrolyte membrane at neutral pH, RSC Adv. 13 (2023) 20235–20242, https://doi.org/10.1039/d3ra02889e.

[57] Y. Tang, K. Fan, I. Herath, W. Gustave, C. Lin, J. Qin, R. Qiu, Contribution of free hydroxyl radical to the formation of micro(nano)plastics and release of additives during polyethylene degradation in water, Environ. Pollut. 337 (2023), https://doi.org/10.1016/j.envpol.2023.122590.